CONDENSED MATTER PHYSICS

Self-consistent determination of spin Hall angle and spin diffusion length in Pt and Pd: The role of the interface spin loss

Xinde Tao[1]*, Qi Liu[1]*, Bingfeng Miao[1,2]*, Rui Yu[1], Zheng Feng[3,4], Liang Sun[1,2], Biao You[1,2], Jun Du[1,2], Kai Chen[5], Shufeng Zhang[5], Luo Zhang[6], Zhe Yuan[6], Di Wu[1,2†], Haifeng Ding[1,2†]

Spin Hall angle (θ_{SH}) and spin diffusion length (λ_{sd}) are the key parameters in describing the spin-charge conversion, which is an integral part of spintronics. Despite their importance and much effort devoted to quantifying them, significant inconsistencies in the reported values for the same given material exist. We report a self-consistent method to quantify both θ_{SH} and λ_{sd} of nonmagnetic materials by spin pumping with various ferromagnetic (FM) pumping sources. We characterize the spin-charge conversion for Pt and Pd with various FM combinations using (i) effective spin-mixing conductance, (ii) microwave photoresistance, and (iii) inverse spin Hall effect measurements and find that the pumped spin current suffers an interfacial spin loss (ISL), whose magnitude varies for different interfaces. By properly treating the ISL effect, we obtained consistent values of θ_{SH} and λ_{sd} for both Pt and Pd regardless of the ferromagnet used.

INTRODUCTION

Pure spin currents carry information with minimum power dissipation because they are not accompanied by net charge currents or stray Oersted fields (1). Thus, the study of pure spin currents has recently attracted great interest (2–9). For the application of novel low-power devices using pure spin currents and their integration with present-day charge-based technologies, an understanding of the interconversion between spin and charge currents is of critical importance. To date, various approaches, including the spin Hall effect (SHE) (10), spin pumping (5), and spin Seebeck effect (6), have been used to obtain pure spin currents. For the detection of a pure spin current, the inverse SHE (ISHE) is the most commonly used method. Overall, the interconversion can be described by $J_S = \frac{\hbar}{2e}\theta_{SH}J_C \times \sigma$ (SHE) and $J_C = \frac{2e}{\hbar}\theta_{SH}J_S \times \sigma$ (ISHE), where $J_{S(C)}$ is the spin (charge) current, $\hbar$ is the reduced Planck's constant, e is the electron charge, σ denotes the direction of spin index, and θ_{SH} is the spin Hall angle, which quantifies the conversion efficiency between charge and spin currents. Typically, the measurement of θ_{SH} is entangled with another important material parameter, the spin diffusion length (λ_{sd}), which quantifies the decay behavior of the pure spin current along with its propagation. Both θ_{SH} and λ_{sd} are critical parameters for spintronic applications, and they can be measured via nonlocal magnetotransport (7), ferromagnetic resonance (FMR)–based spin pumping (8, 11, 12), or spin-torque (ST)–FMR (13, 14). However, significant inconsistencies in the reported values of θ_{SH} and λ_{sd} exist (see section S1) even when the same technique is used. For example, for platinum (Pt), these values scatter by more than one order of magnitude: θ_{SH} values range from 0.01 to 0.20, and λ_{sd} values range from 1 to 10 nm. Recent studies point out that pure spin currents can be depolarized at multilayer interfaces, affecting the estimates of θ_{SH} and λ_{sd} (14–20). The existence of interfacial dissipation of a spin-polarized current was originally proposed and identified as spin memory loss (SML) in the study of current-perpendicular-to-plane (CPP) giant magnetoresistance (21). Rojas-Sánchez et al. (15) combined the SML model with spin pumping measurements and estimated θ_{SH} and λ_{sd} for Pt as 0.056 ± 0.01 and 3.4 ± 0.4 nm, respectively. First-principles calculations confirm that a considerable part of the pumped spin current dissipates at the permalloy (Py)/Pt interface (16). Chen and Zhang (17) revisited the spin pumping theory, including the spin-orbit coupling (SOC) at the interface, and found a discontinuity in the spin current at the interface. Amin and Stiles (19) used a generalized magnetoelectronic circuit to investigate spin transport through the interface and found a similar effect. Considering a parameter denoting the transparency of the interface, Zhang et al. (14) investigated Pt with ST-FMR and reported much larger θ_{SH} values (0.19 ± 0.04) and smaller λ_{sd} values (1.4 ± 0.2 nm). This small spin diffusion length is incompatible with the fundamental spin diffusion theory, in which the spin diffusion length must be larger than the electron mean free path l_{mf} (22, 23). Given a conductivity of 15 or 17 microhm·cm for Pt reported in the two experiments (14, 15), l_{mf} is calculated as 5.2 or 4.6 nm (24), respectively. However, these values are much larger, not smaller, than the reported λ_{sd} value. This reversed relation suggests that accurate measurements of θ_{SH} and λ_{sd} still remain elusive.

Here, we systematically study the spin pumping–induced ISHE for a series of FM/nonmagnetic material (NM) bilayer combinations (where FM = Co, Py, or $Co_{50}Fe_{50}$ denoted as CoFe) as a function of NM layer thicknesses (t_N) via (i) effective spin-mixing conductance $g_{eff}^{\uparrow\downarrow}$, (ii) microwave photoresistance, and (iii) ISHE voltage measurements. We found that the ISHE-generated charge current increases with increasing t_N and saturates at ~40 nm for all three FM/Pt systems. The measured $g_{eff}^{\uparrow\downarrow}$ values also increase with t_N but saturate at a rather small thickness, $t_N \sim 2$ nm, similar to that reported previously (8, 12). However, marked differences between the t_N-dependent $g_{eff}^{\uparrow\downarrow}$ values are found when $t_N < 1.5$ nm for different FM/Pt combinations. When it is assumed that there is a zero spin loss at the interface, the values of θ_{SH} and λ_{sd} rely on the FM/Pt combinations. This inconsistency indicates the importance of spin loss at the interface, as θ_{SH} should be an intrinsic parameter of Pt irrelevant of FM/Pt interfaces. Consistent values of $\theta_{SH} = 0.030 \pm 0.002$ and $\lambda_{sd} = 8.0 \pm 0.5$ nm are obtained for Pt in the three bilayer systems when using a slightly modified model given by Chen and Zhang (17, 18). With the

[1]National Laboratory of Solid State Microstructures and Department of Physics, Nanjing University, 22 Hankou Road, Nanjing 210093, P. R. China. [2]Collaborative Innovation Center of Advanced Microstructures, Nanjing University, 22 Hankou Road, Nanjing 210093, P. R. China. [3]Microsystem and Terahertz Research Center, Chinese Academy of Engineering Physics, Chengdu 610299, P. R. China. [4]Institute of Electronic Engineering, Chinese Academy of Engineering Physics, Mianyang 621999, P. R. China. [5]Department of Physics, University of Arizona, Tucson, AZ 85721, USA. [6]Center for Advanced Quantum Studies and Department of Physics, Beijing Normal University, Beijing 100875, P.R. China.
*These authors contributed equally to this work.
†Corresponding author. Email: hfding@nju.edu.cn (H.D.); dwu@nju.edu.cn (D.W.)

same approach, consistent values of $\theta_{SH} \approx 0.0048 \pm 0.0004$ and $\lambda_{sd} = 7.7 \pm 0.5$ nm are also obtained for Pd in the Py/Pd, Co/Pd, and CoFe/Pd systems. The expected relation of $\lambda_{sd} > l_{mf}$ is confirmed for both Pt and Pd, consistent with the general understanding. Moreover, we also found that both Co/Pd and Py/Pd interfaces are almost transparent to pure spin currents. The finding of highly transparent interfaces has strong potential for spintronic applications.
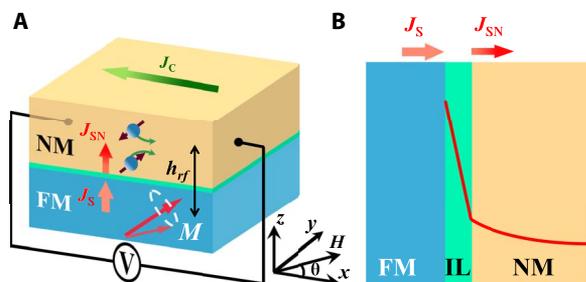
RESULTS AND DISCUSSION
Concept of interface spin loss
Figure 1 presents a schematic of spin pumping and ISHE measurements with an interfacial spin loss (ISL), where panels A and B show the three-dimensional (3D) and cross-sectional views, respectively. Upon radio frequency (rf) excitation, the magnetization of the FM layer precesses and pumps a pure spin current J_S at the FM side of the interface. J_S is partially absorbed at the interface due to the interfacial SOC and disorder (17, 18). This results in a pure spin current with reduced amplitude, J_{SN}, which further diffuses in the NM layer and induces a charge current via the ISHE. The pure spin current absorbed at the interface may also contribute a charge current via the inverse Edelstein effect (25, 26), depending on the strength of the interfacial SOC and disorder. The model is analogous to, but different from, the SML model used by Rojas-Sánchez et al. (15). The SML model uses the external interface parameters estimated from the CPP magnetoresistance study of FM/NM multilayers. As will be shown below, the ISL model self-consistently quantifies the spin loss at the interface via a combination of t_N-dependent $g_{eff}^{\uparrow\downarrow}$ and V_{ISHE}^{SP} measurements only.

Spin pumping–induced voltage, processing angle, and effective spin-mixing conductance
Figure 2 presents typical measurements using Co (20 nm)/Pt (15 nm) (to avoid redundancy, we skip the unit and denote it as Co20/Pt15 hereafter) as an example. We took these types of measurements for a series of FM/NM bilayer combinations as functions of t_N. We measured $V_{ISHE}^{SP}(H)$ for different frequencies (f) at $\theta = 90°$ and $270°$, where the ISHE voltage has a maximum amplitude and the unwanted spin rectification effect is minimized (12, 27). We also demonstrate that self-pumping and thermal effect contribute negligibly to the measured voltage, and the obtained signal is dominated by spin pumping–induced ISHE (see section S2). In addition, we also performed control experiments with CoFeB10/Ta5 and CoFeB10/Pt5. The measured voltage with CoFeB10/Pt5 has the same sign as that with Co/Pt but the opposite sign of that with CoFeB10/Ta5. This also proves that

the measured signals are dominant by spin pumping–induced ISHE because Ta and Pt have opposite signs in the spin Hall angle. As shown in Fig. 2A, the measured curves exhibit symmetric Lorentzian shape and have an opposite sign when H is reversed, as expected for the pure spin pumping–induced ISHE signals. One may notice that the amplitudes are different at different frequencies. The amplitude at 9 GHz is about two times larger than that at 10 and 11 GHz. The spin pumping theory (28), however, predicted that the spin pumping signal should be proportional to f. In addition, the absolute values of the amplitudes are also different at $\theta = 90°$ and $270°$. For example, at 9 GHz, the absolute value is 12.4 μV at $\theta = 90°$, but 9.1 μV at $\theta = 270°$. We find that this is due to the different actual power acting on the sample at different frequencies and different θ values, although the input power is the same. To quantify the active microwave power on the sample, we measured the in- and out-of-plane precession angles of the FM layer (α_1 and β_1, respectively) during spin pumping via microwave photoresistance measurements on the same sample and with the same input microwave power (12). The measured H-dependent microwave photoresistance $\Delta R_{MW}^{F/N}(H)$ for Co20/Pt15 with $f = 9$ GHz at both $\theta = 90°$ and $270°$ are plotted in Fig. 2B. It shows different amplitudes, that is, different α_1 and β_1 for $\theta = 90°$ and $270°$. Together with the anisotropic magnetoresistance measurements, we calculated the product of both precessing angles: $\alpha_1\beta_1$, which is directly proportional to the microwave power acting on the sample. We defined a normalized ISHE signal, which is the ISHE voltage normalized by the precession angles, $\tilde{V}_{ISHE}^{SP}(H) = \frac{V_{ISHE}^{SP}(H)}{\alpha_1\beta_1}$. We plotted the absolute value of the normalized ISHE signal, $\left|\tilde{V}_{ISHE}^{SP}(H)\right|$, for $\theta = 90°$ and $270°$ in Fig. 2C and found that they almost fall into an identical curve, proving that the difference in ISHE voltage is caused by the power difference acting on the sample. To further minimize the residual spin rectification effect, we take the average value of $\left|\tilde{V}_{ISHE}^{SP}(H)\right|$ for $\theta = 90°$ and $270°$ as the amplitude of the signal for the following discussions. After the same normalization process, we also found that the normalized ISHE signals obtained at the resonance field for different frequencies exhibit a linear dependence with f (Fig. 2D), which is consistent with the spin pumping theory (28). We emphasize that the precessing angles can change not only with the reversal of the magnetic field and the variation of f (Fig. 2A) but also with the film thickness, although the same microwave input power is used (29). Therefore, normalizing the ISHE signals with the precessing angles is a critical step in the quantitative study of spin pumping–induced ISHE. This was also recently confirmed by Gupta et al. (30) in an f-dependent study, where they compared different methods to determine the spin Hall angle and found that only this method fulfills the f independence required by dc spin pumping. We fitted the f-dependent resonance magnetic field H_r (Fig. 2E) with the Kittel equation to obtain the effective magnetization M_{eff}. The fitting yields $4\pi M_{eff} = 16500$, 8800, and 21500 Oe for Co, Py, and CoFe, respectively. The obtained effective magnetization is similar to those reported previously (13). Figure 2F shows ΔH - f plots obtained via H-dependent microwave transmission or $V_{ISHE}^{SP}(H)$ for Co20 and Co20/Pt15 samples at different frequencies, where the linear slope yields the damping constants $\alpha_{F/N}$ and α_F. The effective spin-mixing conductance $g_{eff}^{\uparrow\downarrow}$ can then be calculated from the enhanced Gilbert damping, $g_{eff}^{\uparrow\downarrow} = \frac{4\pi M_s t_F}{g\mu_B}(\alpha_{F/N} - \alpha_F)$, where g is the Landé factor and μ_B is the Bohr magneton. We performed the abovementioned measurements

Fig. 1. Schematic of spin pumping and ISHE measurements with the ISL. Upon microwave excitation, the magnetization of the FM layer precesses and pumps a pure spin current into the NM layer and induces a charge current via ISHE. Because of the interfacial spin orbit coupling, the pumped spin current J_S is partially depolarized at the interface, and only part of the spin current J_{SN} propagates in the NM layer. (**A**) 3D view. (**B**) Cross-sectional view.

as functions of t_N for different FM/NM combinations. Because the spin Hall angle and spin diffusion length are the intrinsic properties of the NM layer, they should be independent of the FM material that is used in the spin pumping measurements.

Extraction of θ_{SH} and λ_{sd} of Pt

Figure 3 (A to C) shows the Pt thickness–dependent $g_{eff}^{\uparrow\downarrow}$ for three FM pumping sources: Co20, Py20, and CoFe13. We find that $g_{eff}^{\uparrow\downarrow}$ saturates at about 2 nm in all three systems, although the saturation value of Co/Pt is about half of that for the other two, which is consistent with previous results (14–16). However, we find marked differences when $t_N < 1.5$ nm, as shown in the inserted amplified view. $g_{eff}^{\uparrow\downarrow}$ shows

a progressive increase with t_N for Co/Pt (Fig. 3A), in contrast to the Py/Pt case, where we find a marked jump to an almost saturation value at $t_N \sim 0.3$ nm (Fig. 3B). For CoFe/Pt (Fig. 3C), $g_{eff}^{\uparrow\downarrow}$ shows a behavior in between the abovementioned two cases. The finding of strong differences of t_N-dependent $g_{eff}^{\uparrow\downarrow}$ also suggests that this dependence alone is not the ideal method to extrapolate λ_{sd} because the estimated values are different for different FM/NM combinations, while λ_{sd} should be the intrinsic property of Pt and independent with the used FM.

Figure 3 (D to F) shows the normalized ISHE signal divided by R_N few, namely, $\frac{V_{ISHE}^{SP}}{\alpha_1 \beta_1 R_N few}$, as the function of the Pt thickness t_N, where R_N is the resistance of the NM layer and w is the width of the bilayer
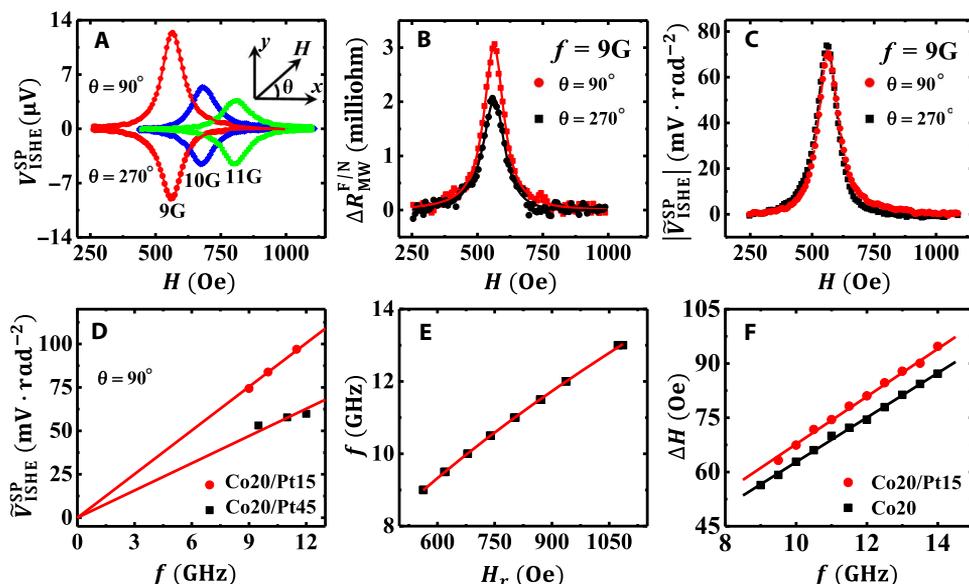
Fig. 2. Detection of spin pumping–induced voltage and characterization of FM/NM interface. (**A**) Representative ISHE voltages V_{ISHE}^{SP} for Co20/Pt15 as a function of H obtained at different frequencies in GHz and at $\theta = 90°$ and $\theta = 270°$. (**B**) H-dependent microwave photoresistance $\Delta R_{MW}^{F/N}$ under the same input microwave power used for the spin pumping measurement ($f = 9$ GHz). (**C**) The absolute value of the spin pumping voltage normalized by the product of two cone angles, $\tilde{V}_{ISHE}^{SP}(H) = V_{ISHE}^{SP}(H)/(\alpha_1 \beta_1)$, at $\theta = 90°$ and $\theta = 270°$. (**D**) f-dependent $\tilde{V}_{ISHE}^{SP}(H)$ at resonance fields for two representative samples, Co20/Pt15 and Co20/Pt45. Symbols are experimental data, and the lines are linear fits. (**E**) f-dependent H_r. Symbols are experimental data, and the line is a fit with Kittel equation. (**F**) Line width (half width at half maximum) of the resonance peak as a function of f for Co20 and Co20/Pt15. The linear fits are overlaid.
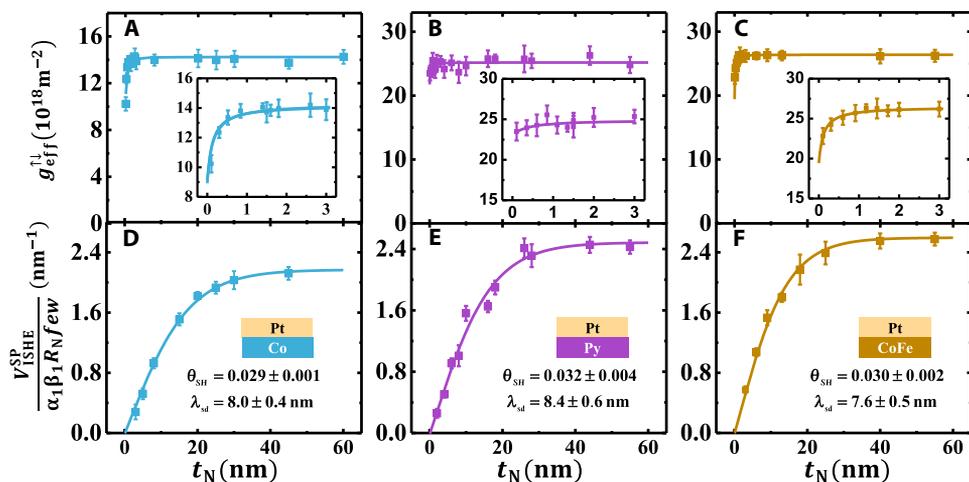
Fig. 3. Extraction of spin Hall angle and spin diffusion length of Pt from different FM/Pt combinations. Pt thickness–dependent $g_{eff}^{\uparrow\downarrow}$ and $\frac{V_{ISHE}^{SP}}{\alpha_1 \beta_1 R_N few}$ for Co20/Pt(t_N), Py20/Pt(t_N), and CoFe13/Pt(t_N). The insets in (**A**) to (**C**) expand $g_{eff}^{\uparrow\downarrow}$ for Pt in the 0- to 3-nm range. Solid lines are fits using Eqs. 1 and 2.

stripe. We note that, in the literature, there is debate about the relation between V_{ISHE}^{SP} and J_c. Some use $V_{ISHE}^{SP} = J_c R_N$ (8, 11, 12), and others use $V_{ISHE}^{SP} = J_c R_{F/N}$ (31, 32), where $R_{F/N}$ is the shunting resistance of both FM and NM layers. We find that our data can be better described by the former relationship because the t_N-dependent $\frac{V_{ISHE}^{SP}}{\alpha_1 \beta_1 R_N few}$ can be described as a hyperbolic tangent function (solid lines), as predicted by the spin pumping theory (28). It can be found that they all have a fast increase when $t_N < 20$ nm and almost reach their saturation values at $t_N \sim$ 40 nm. In addition, they share a very similar characteristic length despite the fact that the saturation values are different. This suggests that these dependences can serve better for the estimation of the spin diffusion length.

To analyze our data, we first assume a zero ISL, as we did previously (12), but found that different values of θ_{SH} were obtained for the Co/Pt and Py/Pt systems. The value for Co/Pt is 0.017, which is ~1.5 times larger than that obtained for Py/Pt, suggesting that the ISL needs to be taken into account to quantify θ_{SH}. We then analyzed our data with the SML model used by Rojas-Sánchez et al. (15) and found that the model failed to explain our data (see section S3). We also attempted to interpret our data with the interface transparency model proposed by Zhang et al. (14), but again failed (see section S4). We therefore continue our data analysis with the ISL model proposed by Chen and Zhang's formalism (17, 18). Because our experimental data show that the measured spin pumping–induced charge voltage is proportional to R_N instead of $R_{F/N}$, we also replace $R_{F/N}$ with R_N. In the model, the precession of the FM layer pumps a pure spin current at the FM side of the interface, J_S, as sketched in Fig. 1. When the spin current crosses the FM/NM interface, it is assumed to lose its amplitude by a factor of δ, and only $(1 - \delta)J_s$ crosses the interface, where δ is the parameter characterizing the ISL and is in between 0 (no loss) and 1 (complete loss). By taking into account both the spin back flow and ISL, it can be estimated that $J_S = \frac{\hbar}{2} G^{\uparrow\downarrow}[1 - (1 - \delta)^2 \varepsilon] f \alpha_1 \beta_1$, where ε is the spin back flow and $G^{\uparrow\downarrow}$ is the spin-mixing conductance. Therefore, the effective spin-mixing conductance at the FM side, which is also $g_{eff}^{\uparrow\downarrow}$ that we measured, can be written as

$$g_{eff}^{\uparrow\downarrow} = G^{\uparrow\downarrow}[1 - (1 - \delta)^2 \varepsilon], \text{ with}$$
$$\varepsilon = G^{\uparrow\downarrow} \Big/ \left[G^{\uparrow\downarrow} + \frac{2}{3} k_F^2 \frac{l_{mf}}{\lambda_{sd}} \tanh\left(\frac{t_N}{\lambda_{sd}}\right) \right] \quad (1)$$

where l_{mf} and k_F are the mean free path and Fermi wave vector of the NM material, respectively. Similarly, we can estimate the actual spin current that flows into Pt as $J_{SN} = \frac{\hbar}{2} G^{\uparrow\downarrow}(1 - \delta)(1 - \varepsilon) f \alpha_1 \beta_1$. The pure spin current can induce a charge voltage, while the lost spin current at the interface could also contribute an additional electric voltage via the inverse Edelstein effect (25, 26). Therefore, the total voltage is composed of the contributions of three parts, originating from the FM layer, the interface, and NM layer. Because Pt is an almost perfect spin sink, we neglected the voltage generated at the FM layer. Then, the measured spin pumping voltage normalized by $\alpha_1 \beta_1 R_N few$ can be simplified as

$$\frac{V_{ISHE}^{SP}}{\alpha_1 \beta_1 R_N few} = G^{\uparrow\downarrow}(1 - \varepsilon)(1 - \delta)\theta_{SH}\lambda_{sd} \tanh\frac{t_N}{2\lambda_{sd}}$$
$$+ \lambda_{IEE} G^{\uparrow\downarrow}\delta(1 + \varepsilon - \delta\varepsilon) \quad (2)$$

where λ_{IEE} is the inverse Edelstein length. We used the experimentally obtained l_{mf} (see section S5) and $k_F = 5.7 \times 10^{10}$ m^{-1} (33) of Pt to perform the fitting with Eqs. 1 and 2 for the data of all three systems shown in Fig. 3. With the parameters listed in Table 1, the fitted curves (solid lines in Fig. 3) reproduce the data for all three systems. The fitted values of θ_{SH} and λ_{sd} agree with each other within the experimental error margin, evidencing the role of the ISL. By averaging these values, we obtained $\theta_{SH} = 0.030 \pm 0.002$ and $\lambda_{sd} = 8.0 \pm 0.5$ nm for Pt. The measured λ_{sd} is longer than the l_{mf} estimated from the resistivity measurements, consistent with the general understanding. Note that the values of θ_{SH} and λ_{sd} of Pt are in agreement with those obtained by first-principles calculations (34), although the predicted giant interface SHE is not observed. The fitted λ_{IEE} value is almost zero (<0.001) in all three systems, which is not too surprising, as λ_{IEE} is not only scaled with the Rashba SOC strength but also influenced by the interface disorder (17). Because our bilayers are fabricated by sputtering, interfacial disorder is expected, and the inverse Edelstein effect could be strongly suppressed, resulting in the negligible value of λ_{IEE}. This may also explain why we did not observe the predicted giant interfacial SHE (34). One may notice that the fitted $G^{\uparrow\downarrow}$ is close to the saturation value of $g_{eff}^{\uparrow\downarrow}$ obtained at large thickness. This can be understood because Pt is an almost perfect spin sink, and the spin backflow is almost 0 at large Pt thickness, resulting in $g_{eff}^{\uparrow\downarrow} \approx G^{\uparrow\downarrow}$ at large thickness (see Eq. 1). We can also catch a glimpse of the amplitude of interface spin loss from the thickness-dependent $g_{eff}^{\uparrow\downarrow}$ at thin thickness (Fig. 3, A to C,

Table 1. Summary of parameters for Pt and Pd obtained by fitting the data in Figs. 3 and 4 and the experimentally measured resistivity (with experimental errors in parentheses).

Parameter (unit)	$G^{\uparrow\downarrow}$ (10^{19} m^{-2})	δ (10^{-2})	θ_{SH} (10^{-3})	λ_{sd} (nm)	λ_{IEE} (10^{-4} nm)	ρ(microhm · cm)	θ_{SH}/ρ(milliohm · cm)$^{-1}$
Co/Pt	1.42 (0.01)	39 (1)	29 (1)	8.0 (0.4)	5.0 (0.6)	19.6 (0.3)	1.47
Py/Pt	2.53 (0.02)	63 (5)	32 (4)	8.4 (0.6)	1.0 (0.2)	21.3 (0.8)	1.50
CoFe/Pt	2.65 (0.08)	53 (2)	30 (2)	7.6 (0.5)	8.0 (0.9)	18.8 (0.5)	1.59
Co/Pd	13.0 (1.4)	0.3 (0.1)	5.0 (0.4)	7.3 (0.4)	3.5 (0.4)	18.7 (0.4)	0.25
Py/Pd	12.9 (2.7)	1.7 (0.9)	5.3 (0.2)	8.0 (0.5)	2.1 (0.8)	21.3 (0.5)	0.27
CoFe/Pd	1.21 (0.03)	30 (5)	4.1 (0.5)	7.5 (0.4)	−41 (5)	15.8 (0.3)	0.26

insets). From Eq. 1, we can easily find that $g_{\text{eff}}^{\uparrow\downarrow}$ would be constant and independent with t_N if the spin current were completely lost at the interface ($\delta = 1$). On the contrary, when there is no interface spin loss, that is, $\delta = 0$, $g_{\text{eff}}^{\uparrow\downarrow}$ will show progressive increase with t_N. Thus, from Fig. 3, we can readily find that δ is the largest in the Py/Pt system and is the smallest in the Co/Pt system, and is consistent with the fitted results (see Table 1).

Extraction of θ_{SH} and λ_{sd} of Pd

To further demonstrate the validity of our approach, we also investigated Pd using the same method of analysis as that used for Pt. Figure 4 shows the measured Pd thickness–dependent effective spin-mixing conductance $g_{\text{eff}}^{\uparrow\downarrow}$ and $\frac{V_{\text{ISHE}}^{\text{SP}}}{\alpha_1\beta_1 R_N few}$ for Co16/Pd, Py16/Pd, and CoFe16/Pd systems. For Co/Pd and Py/Pd, $g_{\text{eff}}^{\uparrow\downarrow}$ increases with increasing Pd thickness and saturates at ~15 nm for both systems, similar to the one reported previously (35). This behavior is quite different from FM/Pt systems, where a fast saturation at ~2 nm was found, suggesting a different spin loss at the interface. The measured $\frac{V_{\text{ISHE}}^{\text{SP}}}{\alpha_1\beta_1 R_N few}$ also increases with increasing Pd thickness and is saturated at ~30 nm for both systems. The saturation thickness for $\frac{V_{\text{ISHE}}^{\text{SP}}}{\alpha_1\beta_1 R_N few}$ is about twice that of the thickness for $g_{\text{eff}}^{\uparrow\downarrow}$ saturation, suggesting that the pure spin current passes through the FM/Pd interface with only a small ISL. For CoFe/Pd, the situation is, however, different with Co/Pd and Py/Pd. $g_{\text{eff}}^{\uparrow\downarrow}$ saturates at a thinner thickness, namely, ~10 nm, and the value obtained at 3 nm is already close to its saturation, suggesting a noticeable ISL in that system. To obtain the quantitative information, we also fitted our experimental data for different FM/Pd combinations using Eqs. 1 and 2. Similarly, we also used the experimentally determined mean free path (see section S5) and the reported $k_F = 9.6 \times 10^9 \text{ m}^{-1}$ of Pd (35) in our fitting. With the parameters listed in Table 1, the fitted curves (solid lines) reproduce the experimental data very well in all three cases. In Py/Pd and Co/Pd systems, we found matched results for spin Hall angle and spin diffusion length ($\theta_{SH} = 0.0051 \pm 0.0003$ and $\lambda_{sd} = 7.7 \pm 0.5$ nm) within the experimental error margin. A slightly smaller spin Hall angle ($\theta_{SH} = 0.0041 \pm 0.0005$) is obtained for the CoFe/Pd system. To check the reliability of the

fitting, we also released the restriction of k_F and used it as a fitting parameter. The best fitting shows that k_F values are similar in all three cases and they are within the 15% difference with respect to the value of $k_F = 9.6 \times 10^9 \text{ m}^{-1}$ that we cited from the literature. The fact that the value of θ_{SH} in the CoFe/Pd system is smaller than in the Co/Pd and Py/Pd systems could be understood with the observed different resistivities (see section S5). The resistivity of Pd in CoFe/Pd is smaller than those in Co/Pd and Py/Pd, which may originate from the relatively smaller lattice mismatch between CoFe and Pd. Wang et al. (34) predicted that θ_{SH} is linearly dependent on ρ for Pt due to the dominant intrinsic mechanism of SHE. This was also recently confirmed experimentally by Sagasta et al. (36). We followed the procedure used by Wang et al. and performed the calculation for Pd and found that the linear dependence of θ_{SH} versus ρ is also valid for Pd (see section S6). Thus, we would expect a constant of θ_{SH}/ρ similar to the behavior of Pt. We calculated this ratio for the investigated three systems and found that they are essentially the same within the error margin (Table 1, last column). This suggests that the intrinsic contribution of SHE is also dominant in pure Pd. We note that our λ_{sd} value matches those reported previously (35, 37). The finding of similar θ_{SH} and λ_{sd} for Pd in three different FM/Pd combinations again illustrates the validity of the ISL model we used for the data analysis. In the CoFe/Pd interface, we also found a noticeable value of λ_{IEE}. In general, λ_{IEE} depends on the spin-orbit interaction and the momentum relaxation time $\lambda_{IEE} = \alpha\tau/\hbar$, where α is the Rashba-type spin-orbit strength which depends on the potential change at the interface, and τ is the momentum relaxation time (26, 38). The smaller lattice mismatch may also yield a sharper interface in CoFe/Pd, a longer τ, and consequently a larger λ_{IEE}. Note that the fitted δ values are very small for both Co/Pd and Py/Pd systems, showing that the two interfaces are almost transparent to pure spin currents. The finding of highly transparent interfaces could be useful for potential applications, such as spin transfer torque–based magnetization switching spintronic devices. For instance, a recent study reports that the switching current densities are similar in Co/Pd and Co/Pt despite their large difference in the spin Hall angle (39). The finding of different ISL values for different interfaces could be understood as follows. As discussed by Liu et al. (16), the ISL results mainly from scattering of the conduction electrons at the abrupt potential change of the interface. Therefore, two factors are essential: the
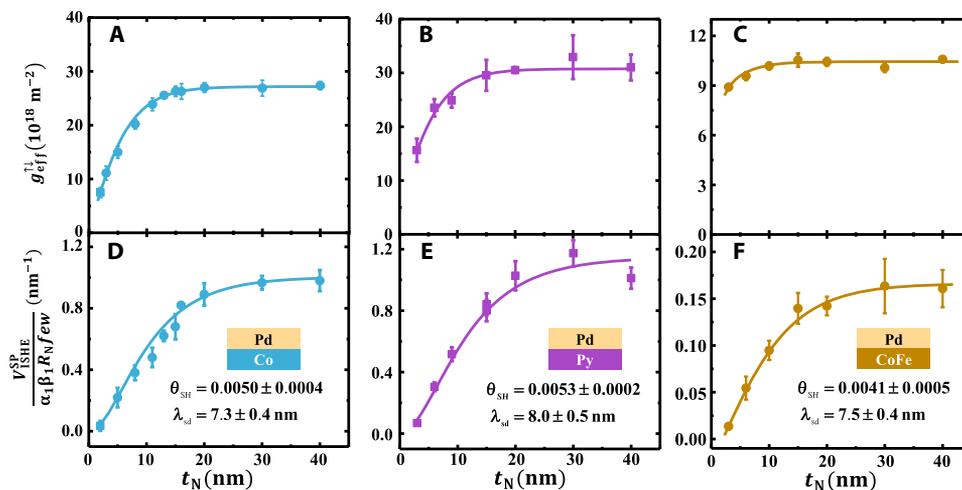
Fig. 4. Extraction of spin Hall angle and spin diffusion length of Pd from different FM/Pd combinations. Pd thickness–dependent $g_{\text{eff}}^{\uparrow\downarrow}$ and $\frac{V_{\text{ISHE}}^{\text{SP}}}{\alpha_1\beta_1 R_N few}$ for Co16/Pd(t_N), Py16/Pd(t_N), and CoFe16/Pd(t_N). Solid lines are fits using Eqs. 1 and 2.

strength of the spin-orbit interaction and the potential gradient at the interface. Because of the strong SOC, the interface spin loss in FM/Pt systems is expected to be strong. In the CoFe/Pd bilayer, although the SOC is relatively weak, the sharp interface allows the conduction electrons to experience a large potential gradient, and thus leads to significant spin loss. Nevertheless, in the Co/Pd and Py/Pd bilayers, the interfaces are not as sharp as those in the CoFe/Pd bilayer. Instead, the interface roughness or the intermixing of atoms near the interface may kill the abrupt potential change, and conduction electrons across the Co/Pd or Py/Pd interface are less scattered, resulting in small interface spin loss.

In the above, we discussed that great care should be taken to estimate θ_{SH} and λ_{sd} because many factors can subtly influence the interpretation of the experimental results. In the following, we also briefly compare the results obtained from spin pumping with those obtained from ST-FMR, where a much higher θ_{SH} was achieved. Experimentally, we repeated the ST-FMR measurements reported by Liu et al. (13) and obtained similar data. Our analysis, however, shows that the symmetrical component of the measured signal is strongly contaminated by the spin pumping–induced ISHE signal. With careful subtraction of the spurious signal, a similar value in θ_{SH}, as compared to the one estimated by spin pumping, is obtained (40).

In summary, using a systematic spin pumping–induced ISHE study of different NM/FM bilayer combinations (NM = Pt and Pd, and FM = Co, Py, and CoFe), we resolve the controversy concerning the quantification of θ_{SH} and λ_{sd}. Marked differences in the t_N-dependent $g_{eff}^{\uparrow\downarrow}$ values are found when $t_N < 1.5$ nm for different FM/Pt combinations, while the normalized ISHE signals $\frac{V_{ISHE}^{SP}}{\alpha_1\beta_1 R_N few}$ show similar t_N dependences. We attribute the difference in t_N-dependent $g_{eff}^{\uparrow\downarrow}$ values to different ISL values at different FM/Pt interfaces. With a slightly modified ISL model proposed by Chen and Zhang, both the t_N-dependent $g_{eff}^{\uparrow\downarrow}$ and $\frac{V_{ISHE}^{SP}}{\alpha_1\beta_1 R_N few}$ can be described with consistent values for Pt ($\theta_{SH} = 0.03$, $\lambda_{sd} = 8.0$ nm) and Pd ($\theta_{SH} = 0.0048$, $\lambda_{sd} = 7.7$ nm), regardless of which FM pumping source is used. The obtained λ_{sd} value is larger than l_{mf} for both Pt and Pd, consistent with the general understanding. Our findings clarify the proper approach to quantify θ_{SH} and λ_{sd}. The approach is demonstrated for Pt and Pd but should also be applicable to other materials. Moreover, we found that both Co/Pd and Py/Pd interfaces are almost transparent to pure spin currents. The finding of highly transparent interfaces has potential for spintronic applications.

MATERIALS AND METHODS

The FM/NM bilayers were deposited sequentially onto GaAs(001) substrates at room temperature by dc magnetron sputtering. They were patterned into stripes of width $w = 20$ μm and length $L = 2.2$ mm using photolithography and liftoff techniques. Coplanar waveguides were patterned with FM/NM stripes placed in the middle of the slots between the signal and ground lines. In such a geometry, the precession of the magnetization was excited with an out-of-plane rf magnetic field of frequency f (7 to 14 GHz). An external magnetic field ($H = 0$ to 1.7 kOe) was applied within the sample plane at an angle θ with respect to the direction of the FM/NM bilayer stripe. The details of the sample fabrication and experimental setup can be found in the studies of Feng et al. (12) and Tao et al. (29). We used the model proposed by Chen and Zhang (17, 18) to account for the ISL in our analysis.

SUPPLEMENTARY MATERIALS

Supplementary material for this article is available at http://advances.sciencemag.org/cgi/content/full/4/6/eaat1670/DC1

section S1. Discrepancy about the measurements of spin Hall angle and spin diffusion length for Pt and Pd

section S2. Negligible contribution of spin rectification effect, self-spin pumping, and thermal effect

section S3. Failure of the fitting with SML model

section S4. Failure of the fitting with interface transparency model

section S5. Thickness-dependent resistivity among different systems

section S6. Calculation of the spin Hall angle of Pd

fig. S1. Spin Hall angle θ_{SH} versus spin diffusion length λ_{sd} for Pt and Pd in literatures.

fig. S2. Comparison of the normalized voltage obtained with single FM layer and FM/Pd bilayer.

fig. S3. Failure of the fitting with SML model.

fig. S4. NM layer thickness dependence of NM resistivity obtained from different combinations.

fig. S5. Calculated spin Hall angle of Pd as a function of temperature.

fig. S6. Calculated spin Hall conductivity and spin Hall angle as a function of resistivity.

table S1. Summary of the parameters used and obtained with the fitting for the data shown in fig. S3.

table S2. Summary of the parameters used and obtained with the fitting for the data shown in fig. S4.

References (41–70)

REFERENCES AND NOTES

1. S. Murakami, N. Nagaosa, S.-C. Zhang, Dissipationless quantum spin current at room temperature. Science 301, 1348–1351 (2003).
2. S. A. Wolf, D. D. Awschalom, R. A. Buhrman, J. M. Daughton, S. von Molnár, M. L. Roukes, A. Y. Chtchelkanova, D. M. Treger, Spintronics: A spin-based electronics vision for the future. Science 294, 1488–1495 (2001).
3. L. Liu, C.-F. Pai, Y. Li, H. W. Tseng, D. C. Ralph, R. A. Buhrman, Spin-torque switching with the giant spin Hall effect of tantalum. Science 336, 555–558 (2012).
4. A. Hamadeh, O. d'Allivy Kelly, C. Hahn, H. Meley, R. Bernard, A. H. Molpeceres, V. V. Naletov, M. Viret, A. Anane, V. Cros, S. O. Demokritov, J. L. Prieto, M. Muñoz, G. de Loubens, O. Klein, Full control of the spin-wave damping in a magnetic insulator using spin-orbit torque. Phys. Rev. Lett. 113, 197203 (2014).
5. Y. Tserkovnyak, A. Brataas, G. E. W. Bauer, Spin pumping and magnetization dynamics in metallic multilayers. Phys. Rev. B 66, 224403 (2002).
6. K. Uchida, S. Takahashi, K. Harii, J. Ieda, W. Koshibae, K. Ando, S. Maekawa, E. Saitoh, Observation of the spin Seebeck effect. Nature 455, 778–781 (2008).
7. S. O. Valenzuela, M. Tinkham, Direct electronic measurement of the spin Hall effect. Nature 442, 176–179 (2006).
8. O. Mosendz, J. E. Pearson, F. Y. Fradin, G. E. W. Bauer, S. D. Bader, A. Hoffmann, Quantifying spin Hall angles from spin pumping: Experiments and theory. Phys. Rev. Lett. 104, 046601 (2010).
9. A. Hoffmann, Spin hall effects in metals. IEEE Trans. Magn. 49, 5172–5193 (2013).
10. M. I. D'yakonov, V. I. Perel, Possibility of orienting electron spins with current. Sov. Phys. JETP Lett. 13, 657 (1971).
11. A. Azevedo, L. H. Vilela-Leão, R. L. Rodríguez-Suárez, A. F. Lacerda Santos, S. M. Rezende, Spin pumping and anisotropic magnetoresistance voltages in magnetic bilayers: Theory and experiment. Phys. Rev. B 83, 144402 (2011).
12. Z. Feng, J. Hu, L. Sun, B. You, D. Wu, J. Du, W. Zhang, A. Hu, Y. Yang, D. M. Tang, B. S. Zhang, H. F. Ding, Spin Hall angle quantification from spin pumping and microwave photoresistance. Phys. Rev. B 85, 214423 (2012).
13. L. Liu, T. Moriyama, D. C. Ralph, R. A. Buhrman, Spin-torque ferromagnetic resonance induced by the spin Hall effect. Phys. Rev. Lett. 106, 036601 (2011).
14. W. Zhang, W. Han, X. Jiang, S.-H. Yang, S. S. P. Parkin, Role of transparency of platinum–ferromagnet interfaces in determining the intrinsic magnitude of the spin Hall effect. Nat. Phys. 11, 496–502 (2015).
15. J.-C. Rojas-Sánchez, N. Reyren, P. Laczkowski, W. Savero, J.-P. Attané, C. Deranlot, M. Jamet, J.-M. George, L. Vila, H. Jaffrès, Spin pumping and inverse spin Hall effect in platinum: The essential role of spin-memory loss at metallic interfaces. Phys. Rev. Lett. 112, 106602 (2014).
16. Y. Liu, Z. Yuan, R. J. H. Wesselink, A. A. Starikov, P. J. Kelly, Interface enhancement of Gilbert damping from first principles. Phys. Rev. Lett. 113, 207202 (2014).
17. K. Chen, S. Zhang, Spin pumping in the presence of spin-orbit coupling. Phys. Rev. Lett. 114, 126602 (2015).
18. K. Chen, S. Zhang, Spin pumping induced electric voltage. IEEE Magn. Lett. 6, 1–4 (2015).
19. V. P. Amin, M. D. Stiles, Spin transport at interfaces with spin-orbit coupling: Formalism. Phys. Rev. B 94, 104419 (2016).

20. M.-H. Nguyen, D. C. Ralph, R. A. Buhrman, Spin torque study of the spin Hall conductivity and spin diffusion length in platinum thin films with varying resistivity. *Phys. Rev. Lett.* **116**, 126601 (2016).

21. A. Fert, S.-F. Lee, Theory of the bipolar spin switch. *Phys. Rev. B* **53**, 6554–6565 (1996).

22. T. Valet, A. Fert, Theory of the perpendicular magnetoresistance in magnetic multilayers. *Phys. Rev. B* **48**, 7099–7113 (1993).

23. J. Bass, W. P. Pratt Jr., Spin-diffusion lengths in metals and alloys, and spin-flipping at metal/metal interfaces: An experimentalist's critical review. *J. Phys. Condens. Matter* **19**, 183201 (2007).

24. N. W. Ashcroft, N. D. Mermin, *Solid State Physics* (Thomson Learning, 1976).

25. J. C. Sánchez, L. Vila, G. Desfonds, S. Gambarelli, J. P. Attane, J. M. De Teresa, C. Magén, A. Fert, Spin-to-charge conversion using Rashba coupling at the interface between non-magnetic materials. *Nat. Commun.* **4**, 2944 (2013).

26. K. Shen, G. Vignale, R. Raimondi, Microscopic theory of the inverse Edelstein effect. *Phys. Rev. Lett.* **112**, 096601 (2014).

27. L. Bai, Z. Feng, P. Hyde, H. F. Ding, C.-M. Hu, Distinguishing spin pumping from spin rectification in a Pt/Py bilayer through angle dependent line shape analysis. *Appl. Phys. Lett.* **102**, 242402 (2013).

28. A. Brataas, G. E. W. Bauer, P. J. Kelly, Non-collinear magnetoelectronics. *Phys. Rep.* **427**, 157–255 (2006).

29. X. D. Tao, Z. Feng, B. F. Miao, L. Sun, B. You, D. Wu, J. Du, W. Zhang, H. F. Ding, The spin Hall angle and spin diffusion length of Pd measured by spin pumping and microwave photoresistance. *J. Appl. Phys.* **115**, 17C504 (2014).

30. S. Gupta, R. Medwal, D. Kodama, K. Kondou, Y. Otani, Y. Fukuma, Important role of magnetization precession angle measurement in inverse spin Hall effect induced by spin pumping. *Appl. Phys. Lett.* **110**, 022404 (2017).

31. P. Deorani, J. Son, K. Banerjee, N. Koirala, M. Brahlek, S. Oh, H. Yang, Observation of inverse spin Hall effect in bismuth selenide. *Phys. Rev. B* **90**, 094403 (2014).

32. K. Ando, E. Saitoh, Observation of the inverse spin Hall effect in silicon. *Nat. Commun.* **3**, 629 (2012).

33. P. Deorani, H. Yang, Role of spin mixing conductance in spin pumping: Enhancement of spin pumping efficiency in Ta/Cu/Py structures. *Appl. Phys. Lett.* **103**, 232408 (2013).

34. L. Wang, R. J. H. Wesselink, Y. Liu, Z. Yuan, K. Xia, P. J. Kelly, Giant room temperature interface spin Hall and inverse spin Hall effects. *Phys. Rev. Lett.* **116**, 196602 (2016).

35. J. Foros, G. Woltersdorf, B. Heinrich, A. Brataas, Scattering of spin current injected in Pd(001). *J. Appl. Phys.* **97**, 10A714 (2005).

36. E. Sagasta, Y. Omori, M. Isasa, M. Gradhand, L. E. Hueso, Y. Niimi, Y. C. Otani, F. Casanova, Tuning the spin Hall effect of Pt from the moderately dirty to the superclean regime. *Phys. Rev. B* **94**, 060412 (2016).

37. O. Mosendz, V. Vlaminck, J. E. Pearson, F. Y. Fradin, G. E. W. Bauer, S. D. Bader, A. Hoffmann, Detection and quantification of inverse spin Hall effect from spin pumping in permalloy/normal metal bilayers. *Phys. Rev. B* **82**, 214403 (2010).

38. S. Zhang, A. Fert, Conversion between spin and charge currents with topological insulators. *Phys. Rev. B* **94**, 184423 (2016).

39. A. Ghosh, K. Garello, C. O. Avci, M. Gabureac, P. Gambardella, Interface-enhanced spin-orbit torques and current-induced magnetization switching of Pd/Co/AlOx layers. *Phys. Rev. A* **7**, 014004 (2017).

40. Q. Liu, Y. Zhang, B. F. Miao, K. He, L. Sun, D. Wu, X. R. Wang, H. F. Ding, *(to be published)*.

41. K. Ando, S. Takahashi, K. Harii, K. Sasage, J. Ieda, S. Maekawa, E. Saitoh, Electric manipulation of spin relaxation using the spin Hall effect. *Phys. Rev. Lett.* **101**, 036601 (2008).

42. K. Ando, S. Takahashi, J. Ieda, H. Kajiwara, H. Nakayama, T. Yoshino, K. Harii, Y. Fujikawa, M. Matsuo, S. Maekawa, E. Saitoh, Inverse spin-Hall effect induced by spin pumping in metallic system. *J. Appl. Phys.* **109**, 103913 (2011).

43. K. Kondou, H. Sukegawa, S. Mitani, K. Tsukagoshi, S. Kasai, Evaluation of spin Hall angle and spin diffusion length by using spin current-induced ferromagnetic resonance. *Appl. Phys. Express* **5**, 073002 (2012).

44. H. Nakayama, K. Ando, K. Harii, T. Yoshino, R. Takahashi, Y. Kajiwara, K. Uchida, Y. Fujikawa, E. Saitoh, Geometry dependence on inverse spin Hall effect induced by spin pumping in Ni81Fe19/Pt films. *Phys. Rev. B* **85**, 144408 (2012).

45. V. Vlaminck, J. E. Pearson, S. D. Bader, A. Hoffmann, Dependence of spin-pumping spin Hall effect measurements on layer thicknesses and stacking order. *Phys. Rev. B* **88**, 064414 (2013).

46. H. Y. Hung, G. Y. Luo, Y. C. Chiu, P. Chang, W. C. Lee, J. G. Lin, S. F. Lee, M. Hong, J. Kwo, Detection of inverse spin Hall effect in epitaxial ferromagnetic Fe3Si films with normal metals Au and Pt. *J. Appl. Phys.* **113**, 17C507 (2013).

47. H. Jiao, G. E. W. Bauer, Spin backflow and ac voltage generation by spin pumping and the inverse spin Hall effect. *Phys. Rev. Lett.* **110**, 217602 (2013).

48. H. L. Wang, C. H. Du, Y. Pu, R. Adur, P. C. Hammel, F. Y. Yang, Scaling of spin Hall angle in 3d, 4d, and 5d metals from Y3Fe5O12/Metal Spin Pumping. *Phys. Rev. Lett.* **112**, 197201 (2014).

49. K. Ando, E. Saitoh, Inverse spin-Hall effect in palladium at room temperature. *J. Appl. Phys.* **108**, 113925 (2010).

50. V. Vlaminck, H. Schultheiss, J. E. Pearson, F. Y. Fradin, S. D. Bader, A. Hoffmann, Mapping microwave field distributions via the spin Hall effect. *Appl. Phys. Lett.* **102**, 199901 (2013).

51. A. Kumar, S. Akansel, H. Stopfel, M. Fazlali, J. Åkerman, R. Brucas, P. Svedlindh, Spin transfer torque ferromagnetic resonance induced spin pumping in the Fe/Pd bilayer system. *Phys. Rev. B* **95**, 064406 (2017).

52. R. Iguchi, E. Saitoh, Measurement of spin pumping voltage separated from extrinsic microwave effects. *J. Phys. Soc. Jpn.* **86**, 011003 (2017).

53. A. Tsukahara, Y. Ando, Y. Kitamura, H. Emoto, E. Shikoh, M. P. Delmo, T. Shinjo, M. Shiraishi, Self-induced inverse spin Hall effect in permalloy at room temperature. *Phys. Rev. B* **89**, 235317 (2014).

54. A. Azevedo, R. O. Cunha, F. Estrada, O. Alves Santos, J. B. S. Mendes, L. H. Vilela-Leão, R. L. Rodríguez-Suárez, S. M. Rezende, Electrical detection of ferromagnetic resonance in single layers of permalloy: Evidence of magnonic charge pumping. *Phys. Rev. B* **92**, 024402 (2015).

55. M. Harder, Y. Gui, C.-M. Hu, Electrical detection of magnetization dynamics via spin rectification effects. *Phys. Rep.* **661**, 1–59 (2016).

56. Y. Tserkovnyak, A. Brataas, G. E. W. Bauer, B. I. Halperin, Nonlocal magnetization dynamics in ferromagnetic heterostructures. *Rev. Mod. Phys.* **77**, 1375–1421 (2005).

57. H. Y. T. Nguyen, W. P. Pratt Jr., J. Bass, Spin-flipping in Pt and at Co/Pt interfaces. *J. Magn. Magn. Mater.* **361**, 30–33 (2014).

58. C. T. Boone, J. M. Shaw, H. T. Nembach, T. J. Silva, Spin-scattering rates in metallic thin films measured by ferromagnetic resonance damping enhanced by spin-pumping. *J. Appl. Phys.* **117**, 223910 (2015).

59. P. Fan, K. Yi, J.-D. Shao, Z.-X. Fan, Electrical transport in metallic films. *J. Appl. Phys.* **95**, 2527–2531 (2004).

60. K. Fuchs, N. F. Mott, The conductivity of thin metallic films according to the electron theory of metals. *Math. Proc. Cambridge Philos. Soc.* **34**, 100–108 (1938).

61. E. H. Sondheimer, The mean free path of electrons in metals. *Adv. Physiol. Educ.* **50**, 499–537 (1952).

62. O. K. Andersen, Z. Pawlowska, O. Jepsen, Illustration of the linear-muffin-tin-orbital tight-binding representation: Compact orbitals and charge density in Si. *Phys. Rev. B* **34**, 5253 (1986).

63. U. von Barth, L. Hedin, A local exchange-correlation potential for the spin polarized case: I. *J. Phys. C Solid State Physics* **5**, 1629 (1972).

64. Y. Liu, A. A. Starikov, Z. Yuan, P. J. Kelly, First-principles calculations of magnetization relaxation in pure Fe, Co, and Ni with frozen thermal lattice disorder. *Phys. Rev. B* **84**, 014412 (2011).

65. Y. Liu, Z. Yuan, R. J. H. Wesselink, A. A. Starikov, M. van Schilfgaarde, P. J. Kelly, Direct method for calculating temperature-dependent transport properties. *Phys. Rev. B* **91**, 220405 (2015).

66. T. Tanaka, H. Kontani, M. Naito, T. Naito, D. S. Hirashima, K. Yamada, J. Inoue, Intrinsic spin Hall effect and orbital Hall effect in 4d and 5d transition metals. *Phy. Rev. B* **77**, 165117 (2008).

67. G. Y. Guo, Ab initio calculation of intrinsic spin Hall conductivity of Pd and Au. *J. Appl. Phys.* **105**, 07C701 (2009).

68. W. Zhang, M. B. Jungfleisch, W. Jiang, Y. Liu, J. E. Pearson, S. G. E. te Velthuis, A. Hoffmann, F. Freimuth, Y. Mokrousov, Reduced spin-Hall effects from magnetic proximity. *Phys. Rev. B* **91**, 115316 (2015).

69. J. P. Perdew, A. Zunger, Self-interaction correction to density-functional approximations for many-electron systems. *Phys. Rev. B* **23**, 5048 (1981).

70. S. H. Vosko, L. Wilk, M. Nusair, Accurate spin-dependent electron liquid correlation energies for local spin density calculations: A critical analysis. *Can. J. Phys.* **58**, 1200–1211 (1980).

ScienceAdvances

Self-consistent determination of spin Hall angle and spin diffusion length in Pt and Pd: The role of the interface spin loss

Xinde Tao, Qi Liu, Bingfeng Miao, Rui Yu, Zheng Feng, Liang Sun, Biao You, Jun Du, Kai Chen, Shufeng Zhang, Luo Zhang, Zhe Yuan, Di Wu and Haifeng Ding

ARTICLE TOOLS	http://advances.sciencemag.org/content/4/6/eaat1670
SUPPLEMENTARY MATERIALS	http://advances.sciencemag.org/content/suppl/2018/06/18/4.6.eaat1670.DC1
REFERENCES	This article cites 68 articles, 3 of which you can access for free http://advances.sciencemag.org/content/4/6/eaat1670#BIBL
PERMISSIONS	http://www.sciencemag.org/help/reprints-and-permissions

Use of this article is subject to the Terms of Service